GEOPHYSICS, VOL. 69, NO. 2 (MARCH-APRIL 2004); P. 489–496, 3 FIGS., 1 TABLE.
10.1190/1.1707069

Grid Euler deconvolution with constraints for 2D structures

M. F. Mushayandebvu*, V. Lesur‡, A. B. Reid**, and J. D. Fairhead§

ABSTRACT

The conventional formulation of 3D Euler deconvolution assumes that the observed field in each Euler window varies in all directions. Where the source is 2D, this assumption leads to the production of poorly constrained solutions. If the source is 2D, the problem leads to a rank deficient normal equations matrix having an eigenvector associated with a zero eigenvalue. This vector lies in the horizontal plane and is pointing along the strike direction, thus allowing for the identification of a 2D structure and its strike. Finding a pseudoinverse via eigenvector expansion allows accurate source location, and the strike information allows the automatic implementation of profile-based techniques like extended Euler deconvolution to gridded data, thus allowing for the first time the estimation of strikes, dips, and susceptibilities from grids using an automatic process. We present a grid-based version of Euler deconvolution that has the ability to define within an Euler operating window whether the source is 2D or 3D in character so that the solutions can be treated differently. We illustrate the new approaches on model and real data.

INTRODUCTION

The use of Euler deconvolution as an interpretation tool to determine source location of potential fields anomalies is well established. Thompson (1982) developed the technique and applied it to profile data, and Reid et al. (1990) developed the more widely used version for grid-based data. Recent improvements in the technique included an automated method to eliminate poorly constrained solutions (Fairhead et al., 1994), the estimation of the structural index (Barbosa et al., 1999), the application to tensor gravity gradient data (Zhang et al., 2000), and the introduction of a second controlling equation allowing determination of susceptibility contrasts and dips from magnetic profile data (Mushayandebvu et al., 2001). This last enhanced capability was termed "extended Euler deconvolution." Nabighian and Hansen (2001) have shown that if a solution of Laplace's equation satisfies Euler's homogeneity equation, so does its generalized Hilbert transform. This gives the second controlling equation of Mushayandebvu et al. (2001), and it leads to the unification of Werner and Euler deconvolution techniques.

The conventional formulation of 3D Euler deconvolution assumes that the observed field in each Euler window is due to a 3D source with a field varying in all directions. Where the source is 2D, we show analytically that the solution will be unstable, resulting in poor solutions which might be rejected by routine techniques for cleaning out poorly constrained solutions (e.g., Fairhead et al., 1994). The unstable solutions are distributed along the strike direction of the 2D structure.

We introduce a new approach to implementing grid Euler deconvolution that has the ability to define within the Euler operating window whether the source is 2D or 3D in character so that the solutions can be treated differently. Finding a pseudoinverse via eigenvector expansion allows accurate source location, and the strike information allows the automatic implementation of profile-based techniques such as extended Euler deconvolution (Mushayandebvu et al., 2001) to gridded data to give dip and susceptibility information. This is (to our knowledge) the first time anyone has shown how to estimate strikes, dips, and susceptibilities from grids using an automatic process.

THEORY

Classic 3D Euler deconvolution and statement of the problem

The 3D equation for Euler deconvolution given by Thompson (1982) is

$$(x-x_o)\frac{\partial T}{\partial x}+(y-y_o)\frac{\partial T}{\partial y}+(z-z_o)\frac{\partial T}{\partial z}=N(B-T), \qquad (1)$$

Published on Geophysics Online October 8, 2003. Manuscript received by the Editor March 18, 2002; revised manuscript received August 14, 2003.
*Formerly University of Leeds, School of Earth Sciences, Leeds LS2 9JT, United Kingdom; presently Image Interpretation Technologies Inc., 210, 333-24th Avenue SW, Calgary, Alberta T2S 3E6, Canada. E-mail: martin@iitech.ca.
‡Formerly University of Leeds, School of Earth Sciences, Leeds LS2 9JT, United Kingdom; presently British Geological Survey, Murchison House, West Mains Road, Edinburgh EH9 3LA, United Kingdom. E-mail: vbfl@bgs.ac.uk.
**Reid Geophysics, 49 Carr Bridge Drive, Leeds LS16 7LB, United Kingdom. E-mail: alan@reid-geophys.co.uk.
§GETECH, c/o University of Leeds, School of Earth Sciences, Leeds LS2 9JT, United Kingdom. E-mail: jdf@getech.leeds.ac.uk.

where (x_0, y_0, z_0) is the position of a source whose total field T is detected at (x, y, z), and B and N are the regional value of the field and the structural index, respectively. For a contact model the right side of the equation reduces to an offset, A, which incorporates amplitude, strike, and dip factors (Reid et al., 1990).

To solve for the source location, the process normally involves writing equation (1) in matrix form, for each window with n data points, i.e.,

$$\begin{bmatrix} \frac{\partial T}{\partial x_1} & \frac{\partial T}{\partial y_1} & \frac{\partial T}{\partial z_1} & N \\ \vdots & \vdots & \vdots & \vdots \\ \vdots & \vdots & \vdots & \vdots \\ \frac{\partial T}{\partial x_n} & \frac{\partial T}{\partial y_n} & \frac{\partial T}{\partial z_n} & N \end{bmatrix} \begin{bmatrix} x_o \\ y_o \\ z_o \\ B \end{bmatrix}$$

$$= \begin{bmatrix} x_1 \frac{\partial T}{\partial x_1} + y_1 \frac{\partial T}{\partial y_1} + z_1 \frac{\partial T}{\partial z_1} + NT_1 \\ \vdots \\ \vdots \\ x_n \frac{\partial T}{\partial x_n} + y_n \frac{\partial T}{\partial y_n} + z_n \frac{\partial T}{\partial z_n} + NT_n \end{bmatrix}, \quad (2)$$

where $\frac{\partial T}{\partial x_i}$ represents $\frac{\partial T}{\partial x}|_{x=x_i}$, and similarly for the other gradients.

Equation (2) is of the form

$$\mathbf{Am} = \mathbf{d}. \quad (3)$$

The least-squares solution of the overdetermined case involves solving the normal equations

$$\mathbf{A}^T\mathbf{Am} = \mathbf{A}^T\mathbf{d}, \quad (3)$$

leading to a solution

$$\mathbf{m} = (\mathbf{A}^T\mathbf{A})^{-1}\mathbf{A}^T\mathbf{d}, \quad (4)$$

where $(\mathbf{A}^T\mathbf{A})^{-1}$ is the inverse of $(\mathbf{A}^T\mathbf{A})$, and $(\mathbf{A}^T\mathbf{A})^{-1}\mathbf{A}^T$ is sometimes called the least-squares inverse of $\mathbf{A}$ (e.g., Menke, 1989).

Ideal 2D features running parallel to an axis will produce a column of zeros in matrix $\mathbf{A}$, and one cannot solve for the source location. More generally, for ideal 2D features, the ratio of the horizontal derivatives $(\frac{\partial T}{\partial x}/\frac{\partial T}{\partial y})$ is a constant related to the strike of the feature. Thus, two columns in matrix $\mathbf{A}$ are linearly dependent. This implies that $\mathbf{A}^T\mathbf{A}$ will also have two columns, which are linearly dependent and becomes singular [i.e., $(\mathbf{A}^T\mathbf{A})^{-1}$ does not exist], and so the least-squares solution [equation (4)] cannot be calculated. Stated in terms of eigenvectors and eigenvalues, the matrix $\mathbf{A}^T\mathbf{A}$ will have an eigenvector associated with a zero eigenvalue, pointing along the strike direction, the direction along which the gradient of the field is zero.

Finding a pseudoinverse via eigenvector expansion

Eigenvector expansion gives a way of solving the normal equations when $\mathbf{A}^T\mathbf{A}$ has zero eigenvalues and is described in texts such as Forsythe et al. (1977) and Naidu and Mathew (1998). The normal equations matrix $\mathbf{A}^T\mathbf{A}$ is square and symmetric, so its eigenvectors are orthogonal. Let $\mathbf{V}$ be a matrix whose columns are the eigenvectors of $\mathbf{A}^T\mathbf{A}$ and Λ be a diagonal matrix with the eigenvalues. Then

$$\mathbf{A}^T\mathbf{A} = \mathbf{V}\Lambda\mathbf{V}^T. \quad (5)$$

The inverse of Λ, Λ^{-1} is the diagonal matrix whose elements are the reciprocals of the eigenvalues. If $\mathbf{A}^T\mathbf{A}$ is not singular, the inverse of $(\mathbf{A}^T\mathbf{A})$ is given by

$$(\mathbf{A}^T\mathbf{A})^{-1} = \mathbf{V}\Lambda^{-1}\mathbf{V}^T. \quad (6)$$

When an eigenvalue is zero, the inverse, Λ^{-1}, is not defined. However, a generalized inverse can always be constructed by replacing the offending reciprocals with zeros. The solution thus obtained represents the minimum norm solution.

Identification of 2D structures in data

The normal equation matrix given in equation (3) has four eigenvectors. In the full rank case, the field is due to a 3D source, and there exists a unique and stable solution to the system of equations. If the source is 2D, the matrix $\mathbf{A}^T\mathbf{A}$ is rank deficient, having an eigenvector associated with a zero eigenvalue. This vector lies in the horizontal plane and is pointing along the strike directions. Therefore, using data points from an Euler window, one can build the $\mathbf{A}$ matrix and compute the $\mathbf{A}^T\mathbf{A}$ eigenvalues, and hence identify a 2D structure and its strike when a zero eigenvalue is associated with an eigenvector in the horizontal xy plane.

In the presence of noise in the data, a 2D structure is associated with a small nonzero eigenvalue, and the corresponding eigenvector is not exactly aligned with the geological strike. Therefore, if the same scheme as above is used for identifying 2D structures, two key points need to be addressed: what will be the eigenvalues associated with a 2D structure, and how can we obtain the strike direction from the associated eigenvector?

In the Appendix, we show that if data are contaminated with Gaussian noise with a zero mean, the eigenvalue $\lambda = 0$ is raised to $\lambda \cong n\sigma^2$, where n is the number of points in the Euler window and σ^2 is the variance of the noise in the x and y directions. The orthogonal projection $\tilde{\mathbf{V}}$ of the associated eigenvector which is almost in the xy plane onto this plane can be selected as a strike direction if

$$\tilde{\mathbf{v}}^T(\mathbf{A} + \delta\mathbf{A})^T(\mathbf{A} + \delta\mathbf{A})\tilde{\mathbf{v}} \cong n\sigma^2, \quad (7)$$

where $\delta\mathbf{A}$ is the perturbation of the matrix $\mathbf{A}$ due to noise in the three components of the gradient of the field.

The above results hold for an ideal 2D structure producing observations corrupted with zero-mean Gaussian noise. In practice, the noise or error associated with the Euler equations is large, correlated, and not Gaussian. A practical way of choosing zero eigenvalues and strike directions for real data is described in the sections on application to data.

Methodology

The recommended approach to implementing Euler deconvolution is a modification of the grid approach of Reid et al.

(1990). Only the additional steps are presented. For each Euler window:

1) Compute the $\mathbf{A}^T\mathbf{A}$ eigenvalues and eigenvectors.
2) Assess if source is primarily 2D or 3D. Two-dimensional structures are identified as having a near-zero eigenvalue and an eigenvector almost in the xy plane. Definition of "near-zero" eigenvalue entails either an initial pass over the whole data set mapping the variation of the minimum eigenvalue or assuming a predetermined empirical value as the limit.
3) For all windows, matrix inversion by eigenvector expansion is used to give the minimum norm solution.
4) For sources deemed to be 2D, implementation of extended Euler deconvolution (Mushayandebvu et al., 2001) gives dip and susceptibility information.

APPLICATION TO MODEL DATA

The application of the new approach to Euler deconvolution is illustrated on magnetic data over a model dike with local field settings and strike direction (Table 1) similar to those of the Great Dyke of Zimbabwe used in the section below on application to real data. Grids of the total magnetic intensity and gradients were calculated, and Gaussian noise with a zero mean and a standard deviation of 1.3×10^{-4} nT/m, which is 0.1% of the maximum of the vertical gradient, was added to all grids. A grid cell size of 100 m was used. The total magnetic intensity is presented in Figure 1a.

Deconvolution

Figure 1b shows a histogram of the smallest eigenvalues obtained from the application of Euler deconvolution to the model data using a data window of size 20×20 data points and moving in steps of one grid-cell size. The histogram is a plot of the number of eigenvalues falling within an interval of 5.7×10^{-8} nT^2/m^2 versus the position of the center of the interval. The figure shows that the eigenvalue equal to zero associated with 2D structures is raised to values that peak around $n\sigma^2 = 6.8 \times 10^{-6}$ nT^2/m^2 as predicted above. Though the peak of the curve is easy to pick out, it does not represent the cutoff point for discriminating between 2D and 3D structures, since there is a scatter of points around it. The curve suggests a higher value for the cutoff point around 8.5×10^{-6}. nT^2/m^2 Since there is no sharp cutoff point, a parameter related to the easier-to-pick peak of the curve would be of more practical value. Defining the eigenvalues less than double the value of the peak on the graph (i.e., 13.6×10^{-6} nT^2/m^2 for the model) as being near-zero values was empirically found to work well as a cutoff value. This approach requires running the deconvolution process twice, initially to obtain the histogram of the smallest eigenvalues and then, after analysing it, rerun to solve for source parameters.

Table 1. Model dike parameters and field settings for the model and the Great Dyke.

Field strength	32 000 nT
Field inclination	−55°
Field declination	−10°
Model strike direction azimuth	30°
Model susceptibility (SI units) × thickness (m)	2
Model depth to top	300 m
Model dip to the east	70°

The results of the deconvolution are presented from a decimated solution set obtained by moving the Euler window in steps of four times the grid-cell size. Figure 1c shows the strike and dip directions for 2D solutions. Solutions align perfectly, estimating all model parameters with standard deviation less than 0.05% of the respective mean. The spacing between the solutions represents displacement along strike of the Euler window. Figure 1d is used to illustrate the effects of treating data from windows assessed to represent 2D structures as 3D (i.e., the conventional approach). The × signs represent the true location of the source determined from using the new approach to the deconvolution process, and the dots show the solutions when using the conventional approach. Even though there is some spraying of solutions when using the conventional approach, the two methods produced virtually the same source locations. The main benefit from the new approach is the dip and susceptibility information coming from the grid implementation of extended Euler deconvolution.

APPLICATION TO REAL DATA

The application of the new approaches in Euler deconvolution to real data is illustrated on aeromagnetic data over a section of the Great Dyke of Zimbabwe, targeting shallow sources. The primary objective is to illustrate practical implementation considerations while demonstrating the application of extended Euler deconvolution to grid data.

GREAT DYKE OF ZIMBABWE

Brief geology.—The Great Dyke stands out as a prominent feature cutting across the Archaean Zimbabwe craton. The dike is 550 km long and up to 11 km wide, and extends in a north-northeast-trending direction from the Limpopo Belt in the south into the Zambezi Belt in the north. It is not a true dike but, at its present erosion level, it is the remains of a number of elongated synclinally layered mafic igneous complexes emplaced along a line of weakness in the Earth's crust (Worst, 1960; Wilson and Prendergast, 1988). These complexes pass downward into true dike feeders to the complexes (Podmore and Wilson, 1987). Each complex consists of layered cyclic petrogenetic units with the layering plunging gently towards the center.

Running nearly parallel to the Great Dyke for its entire length are its true dike satellites: the Umvimeela (to the west) and the East dikes (to the east). The satellite dikes are essentially vertical, with a mean dip of 84° towards the Great Dyke for the Umvimeela dike and 89° away from the Great Dyke for the East dike and with average widths of 200 m and 100 m, respectively (Mushayandebvu, 1995).

Magnetic data.—The whole of Zimbabwe has been covered by an aeromagnetic survey program funded by the Canadian International Development Agency. The survey was carried out at a mean terrain clearance of 305 m with traverse lines spaced 1 km apart and tie lines every 14 km. The data were made available by the Geological Survey of Zimbabwe in grid form with a cell size of 125 m. Figure 2a shows a color shaded relief image of a window from the data set used in this study. It highlights the Great Dyke with the edges standing out as highs.

One of the satellite dikes of the Great Dyke, the Umvimeela dike, clearly stands out with a strong anomaly. The other satellite dike, the East dike, comes out with a weaker signature. The magnetic highs appearing at the southeastern corner of the image are associated with mafic units within greenstone belts. Flight-line breaks produced by the gridding routine can be seen on the signature of 2D structures.

Deconvolution.—Euler deconvolution was carried out using a window size of 10 × 10 data points. Initially the Euler window was moved in steps of four times the grid-cell size to gather eigenvalues. Figure 2b is a graph showing the number of eigenvalues falling within an interval of 9.4×10^{-6} nT^2/m^2 versus the position of the center of the interval. The histogram is not symmetrical, as predicted in the Appendix. The behavior of the curve could be explained as a superposition of two causes: the presence of random noise in data, and the fact that in the real world 2D structures are always approximate, that is, they are always discontinuous and irregular (presenting variable thickness). The first cause produces a symmetrical behavior on the histogram, whereas the second imposes an exponential decay. The exponential decay implies there is no obvious clear cut off in the histogram to use for defining near-zero eigenvalues, but the peak is still easy to pick out. A nonoptimal empirical approach is to choose the values less than double the peak on the histogram as near-zero values, which

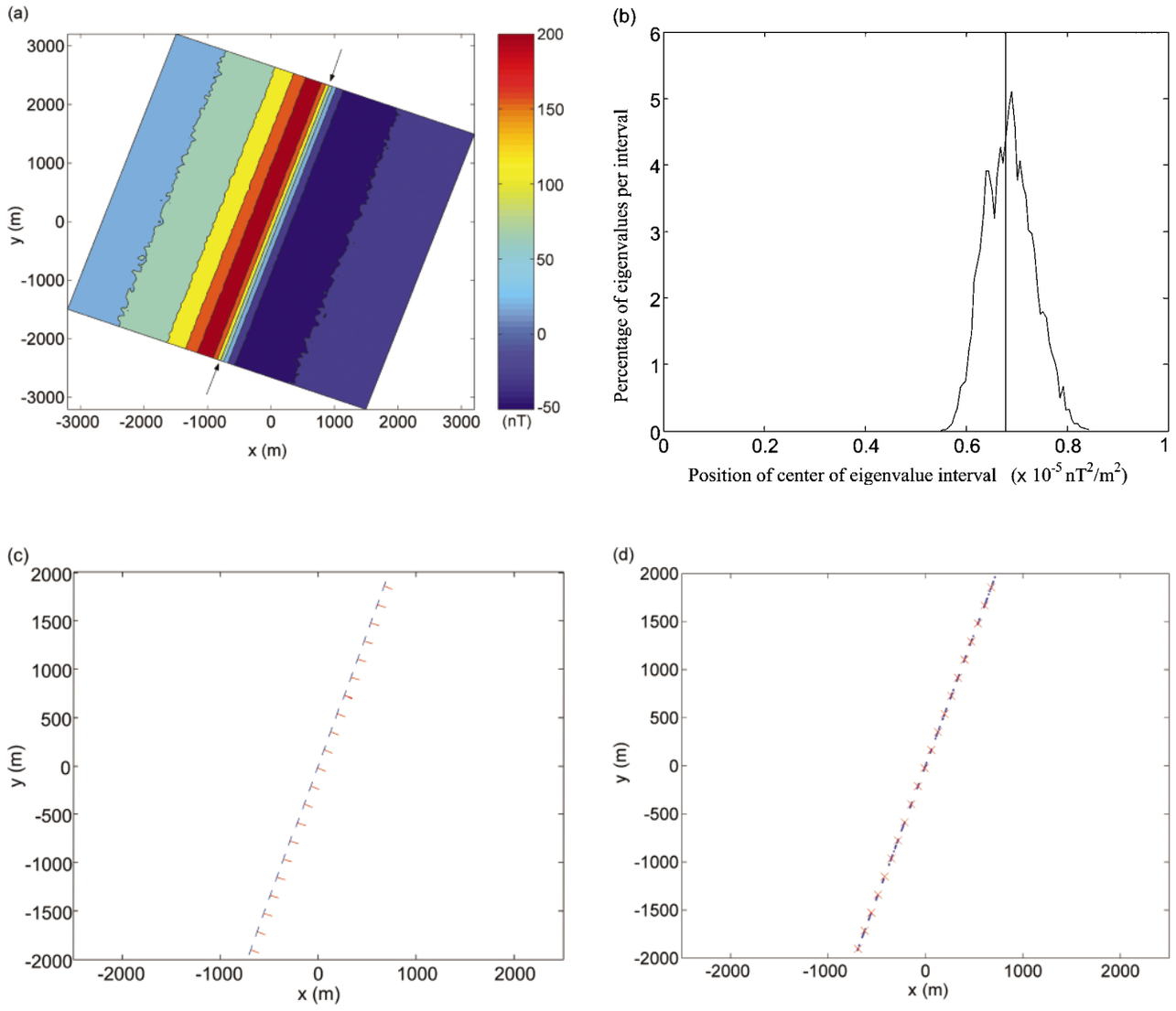

Figure 1. Data and results of the new approach to Euler deconvolution on model data over a thin dike. (a) Total magnetic intensity. Arrows mark approximate location of the dike. (b) Graph of the smallest eigenvalues. Vertical line marks $n\sigma^2 = 6.8 \times 10^{-6}$ nT^2/m^2, showing the level where the zero eigenvalue is raised to by adding random noise. (c) Strike (in blue) and dip (in red) from 2D solutions. (d) Source location from 2D solutions (marked in red) with solutions obtained from treating the same data windows as due to 3D sources (marked in blue).

works for ideal 2D structures. In the above example, this gives a value of 1×10^{-4} nT^2/m^2. It has been observed that for most data sets, there is little variation in this value, and we tend to keep it fixed and avoid recalculating it in order to speed up the deconvolution.

Figures 2c and 2d show the solution space from conventional Euler deconvolution and the new approach, respectively. Only solutions satisfying the inequality

$$\frac{\sigma_{z_0}}{z_0} < 0.06, \tag{8}$$

where z_0 is the estimate of the depth and σ_{z_0} is its standard deviation, have been accepted. Comparison of the two images shows that though the new approach has a better image, the

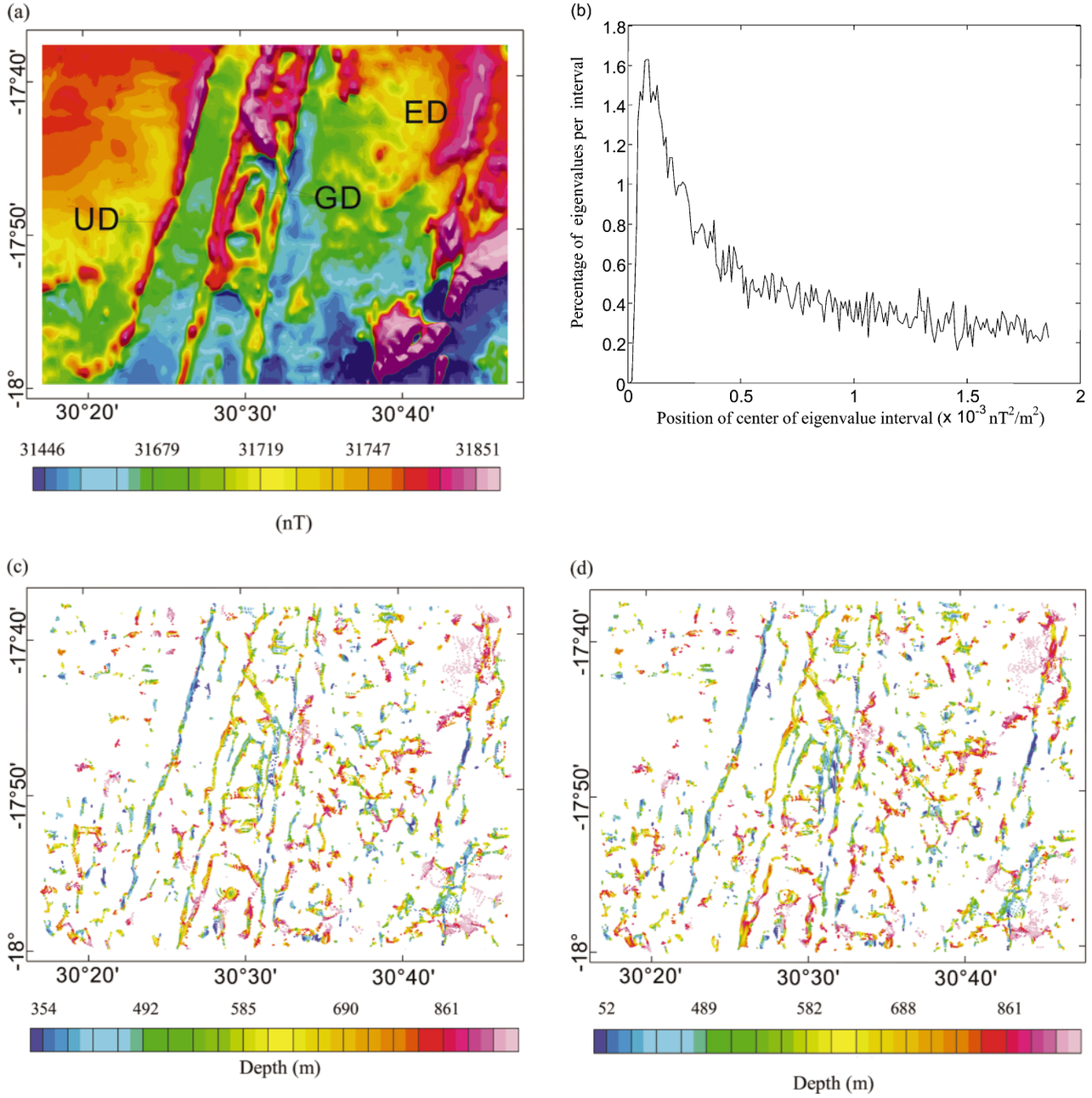

Figure 2. Data and results from Euler deconvolution over a section of the Great Dyke, Zimbabwe. (a) Total magnetic intensity. GD, UD, and ED mark the Great Dyke, the Umvimeela dike, and the East dike, respectively. (b) Graph of the smallest eigenvalues. Source location and depths (from a flight height of 305 m) are presented for conventional Euler deconvolution (c) and the new approach (d) using a structural index of 1.

differences, with the quality of data used, tend to be subtle and not of much significance for a regional interpretation of the data.

Extended Euler deconvolution on grids.—The new approach to Euler deconvolution allows for the implementation of the extended Euler technique to Euler windows identified to be caused by 2D structures.

The characteristics of the present earth field in the area are given in Table 1. The source location results obtained from extended Euler deconvolution, as for conventional Euler, are independent of the presence of remanence, but the estimation of dips and susceptibility values assume a zero remanence. For the Great Dyke and its satellites, the component of the remanence in the plane perpendicular to the dike is very close in direction to that of the present geomagnetic field (McElhinny and Gough, 1963; Mushayandebvu, 1991). The dike anomalies could be modeled either as caused by remanent and induced, magnetization or as fully induced. If the magnetization is assumed to be induced, then higher susceptibilities are

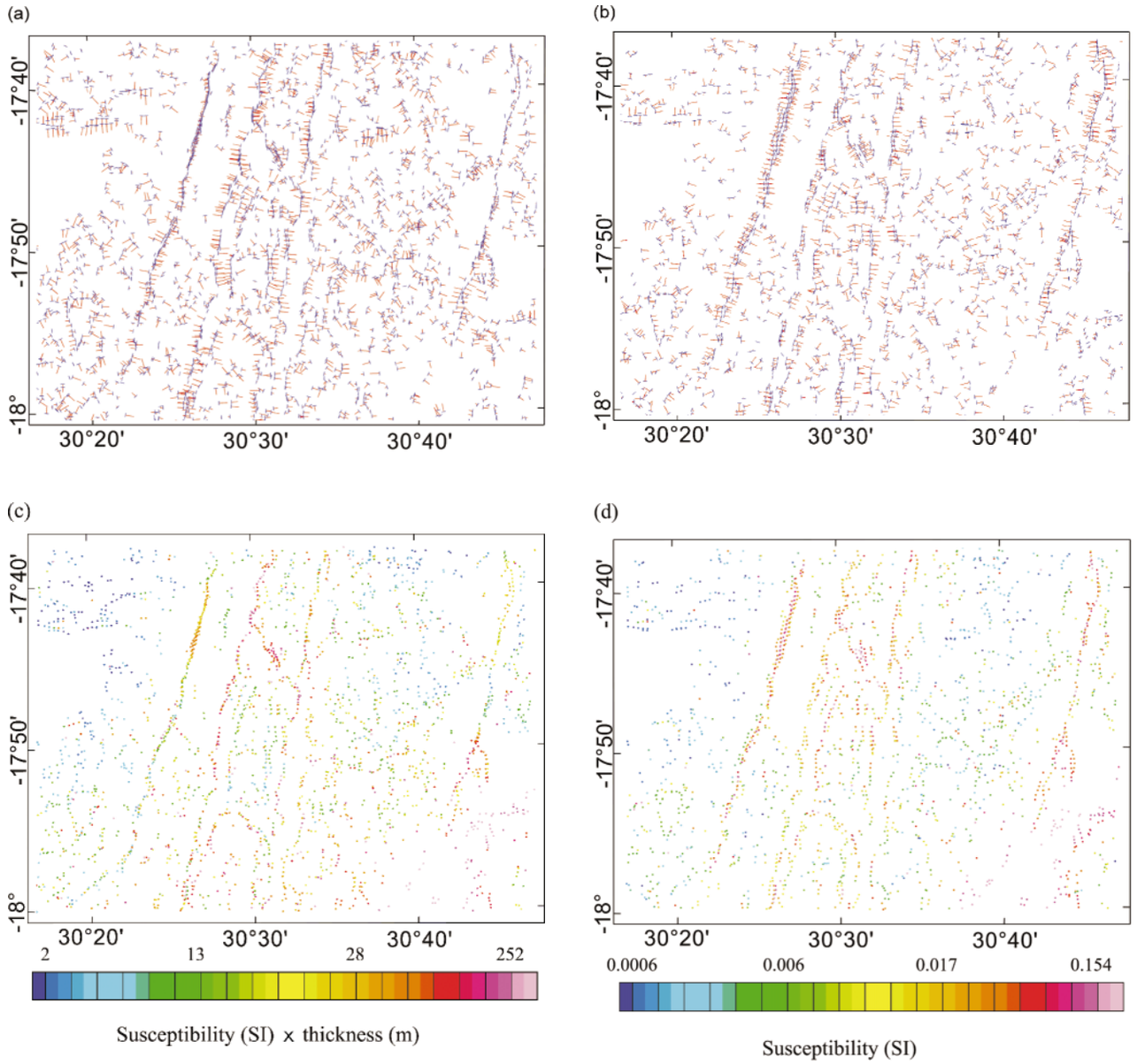

Figure 3. Extended Euler deconvolution results over a section of the Great Dyke. (a) Strike directions (in blue) and dips (in red) for dike models (structural index of 1). The length of the red line is proportional to the cosine of the dip. (b) Strike directions (in blue) and dips (in red) for contact models (structural index of 0). (c) Susceptibility (SI units) times thickness (m) values from dike models. (d) Susceptibility contrast values (SI units) from contact models.

obtained. Estimation of susceptibilities using extended Euler deconvolution assumes zero remanence.

Extended Euler deconvolution assumes either a contact or a dike source model (i.e., uses a structural index of either 0 or 1, respectively). The application of extended Euler deconvolution creates a large volume of information. The full realization of its value depends on the display facilities available.

Figure 3a and 3b show the strike and dip information from the application of extended Euler deconvolution. The extended Euler information is presented for a solution set obtained by moving the Euler window in steps of four grid cell sizes in order to avoid clustering of the images.

When modeled as dikes, both the Umvimeela and East dikes come out essentially vertical with some local variations. The Great Dyke is too wide for the size of the Euler window used for it to be imaged as a thin dike. The edges of the Great Dyke are imaged nicely as thin dikes, but the dips associated with them do not make geological sense.

Modeled as contacts (Figure 3b) , the dips associated with the Umvimeela dike spray both to the east and west, and also a decrease in the clustering of the solutions clearly indicate an inappropriate selection of the structural index. The dip information for the East dike shows more variation than those obtained with the correct index, though this is not as striking as for the Umvimeela dike. The edges of the Great Dyke are better imaged as contacts generally dipping towards the center of the dike.

Figures 3c and 3d show the susceptibility information from extended Euler deconvolution for structural indices of one and zero, respectively. The susceptibility (SI units) $\times$ thickness (m) values for the Umvimeela dike peak around 30 m $\times$ SI units. This is close to a result of 53 ± 6 m $\times$ SI units obtained by Mushayandebvu et al. (2001) from a single profile. For the Great Dyke, the peak of the susceptibility values is around 0.02 (SI units), an acceptable value for a mafic igneous complex.

CONCLUSION

Conventional grid-based Euler deconvolution when implemented on data generated from idealized 2D models gives unstable solutions, which spray along the strike direction of the 2D structure. A method for reducing the spraying when mapping 2D structures is presented and recommended for routine application. The new approach allows for the identification and separation of 2D and 3D source structures. Finding a pseudoinverse via eigenvector expansion allows accurate source location, and the strike information for 2D structures allows the automatic implementation of profile-based techniques such as extended Euler deconvolution to gridded data to work out dips and susceptibility contrasts.

ACKNOWLEDGMENTS

The authors thank the British Natural Environment Research Council for the Realizing Our Potential Award scheme to JDF which partly funded MFM. We thank Associate Editor J. B. C. Silva and two anonymous reviewers for their comments, which led to substantial improvements to the paper.

APPENDIX

IDENTIFICATION OF 2D STRUCTURES IN DATA

Suppose the data are contaminated with a Gaussian noise with a zero mean and that λ and $\mathbf{v}$ are, respectively, an eigenvalue and an eigenvector of the noise-free symmetric matrix $\mathbf{G} = \mathbf{A}^T\mathbf{A}$:

$$\mathbf{G}\mathbf{v} = \lambda\mathbf{v}. \tag{A-1}$$

For a small perturbation of the matrix $\mathbf{G}$, both the eigenvalues and eigenvectors are modified, giving

$$(\mathbf{G} + \delta\mathbf{G})(\mathbf{v} + \delta\mathbf{v}) = (\lambda + \delta\lambda)(\mathbf{v} + \delta\mathbf{v}). \tag{A-2}$$

Then, neglecting the second order in perturbation, we can write

$$\delta\mathbf{G}\mathbf{v} + \mathbf{G}\delta\mathbf{v} \cong \lambda\delta\mathbf{v} + \delta\lambda\mathbf{v}. \tag{A-3}$$

We can chose a normalization for the vector $\mathbf{v} + \delta\mathbf{v}$ such that $\mathbf{v}$ and $\delta\mathbf{v}$ verify $\|\mathbf{v}_2\| = 1$ and $\mathbf{v}^T\delta\mathbf{v} = 0$. In this case, multiplying equation (A-3) on the left by $\mathbf{v}^T$ leads to

$$\mathbf{v}^T\delta\mathbf{G}\mathbf{v} + \mathbf{v}^T\mathbf{G}\delta\mathbf{v} \cong \delta\lambda. \tag{A-4}$$

Since $\mathbf{G}$ is symmetric, the following set of equalities holds:

$$\mathbf{v}^T\mathbf{G}\delta\mathbf{v} = \mathbf{v}^T\mathbf{G}^T\delta\mathbf{v} = \lambda\mathbf{v}^T\delta\mathbf{v} = 0. \tag{A-5}$$

Therefore, we obtain

$$\mathbf{v}^T\delta\mathbf{G}\mathbf{v} \cong \delta\lambda. \tag{A-6}$$

If $\lambda_0 = 0$. replacing $\mathbf{G}$ by $\mathbf{A}^T\mathbf{A}$ leads to $\mathbf{A}\mathbf{v}_0 = \mathbf{v}_0^T\mathbf{A}^T = 0$ and, via equation (A-6), we have

$$\mathbf{v}_0^T(\mathbf{A} + \delta\mathbf{A})^T(\mathbf{A} + \delta\mathbf{A})\mathbf{v}_0 = \mathbf{v}_0^T\delta\mathbf{A}^T\delta\mathbf{A}\mathbf{v}_0 \cong \delta\lambda_0, \tag{A-7}$$

where $\delta\mathbf{A}$ is the perturbation of the matrix $\mathbf{A}$ due to random variables (noise) in the three components of the gradient of the field. Suppose that $\mathbf{v}_0$ is in the xy plane and the noise in the x and y directions are uncorrelated and have the same variance σ^2. Then, from the properties of the χ^2 distributions, it follows that on average

$$\mathbf{v}_0^T\delta\mathbf{A}^T\delta\mathbf{A}\mathbf{v}_0 = n\sigma^2, \tag{A-8}$$

where n is the number of data points in the Euler window. One can see that because of the noise, the eigenvalue $\lambda_0 = 0$ is raised to an average of $\lambda_0 \cong n\sigma^2$.

We now have to define a selection criterion for a strike direction. If a small eigenvalue is associated with an eigenvector $\mathbf{v}$, almost in the xy plane, the orthogonal projection $\tilde{\mathbf{v}}$ of this vector on the xy plane can be calculated. From equation (A-6), this direction can be selected as the strike direction if

$$\tilde{\mathbf{v}}^T(\mathbf{A} + \delta\mathbf{A})^T(\mathbf{A} + \delta\mathbf{A})\tilde{\mathbf{v}} \tag{A-9}$$

is close enough to $n\sigma^2$, where σ^2 is defined as in equation (A-8).

REFERENCES

Barbosa, V. C. F., Silva, J. B. C., and Medeiros, W. E., 1999, Stability analysis and improvement of structural index estimation in Euler deconvolution: Geophysics, **64**, 48–60.

Fairhead, J. D., Bennett, K. J., Gordon, D. R. H., and Huang, D., 1994, Euler: Beyond the "Black Box": 64th Annual International Meeting, SEG, Expanded Abstracts, 422–424.
Forsythe, G. E., Malcolm, M. A., and Moler, C. B., 1977, Computer methods for mathematical computations: Prentice-Hall, Inc.
Menke, W, 1989, Geophysical data analysis: Discrete inverse theory: Academic Press Inc.
McElhinny, M. W., and Gough, D. I., 1963, The palaeomagnetism of the Great Dyke of Southern Rhodesia: Geophysical Journal, **7**, 287-303.
Mushayandebvu, M. F., 1991, A palaeomagnetic study of mafic intrusions associated with the Great Dyke, Zimbabwe: Ph.D. thesis, University of Zimbabwe.
———1995, Magnetic modelling of the Umvimeela and East dykes: Evidence for regional tilting of the Zimbabwe craton adjacent to the Limpopo Belt: Journal of Applied Science in Southern Africa, **1**, 47–58.
Mushayandebvu, M. F., van Driel, P., Reid, A. B., and Fairhead, J. D., 2001, Magnetic source parameters of two-dimensional structures using extended Euler deconvolution: Geophysics, **66**, 814–823.
Nabighian, M. N., and Hansen, R. O., 2001, Unification of Euler and Werner deconvolution in three dimensions via the generalized Hilbert transform: Geophysics, **66**, 1805–1810.
Naidu, P. S., and Mathew, M. P., 1998, Analysis of geophysical potential fields: A digital processing approach: Elsevier Science Publishing Co.
Podmore, F., and Wilson, A. H., 1987, A reappraisal of the structure, geology and emplacement of the Great Dyke, Zimbabwe, *in* Halls H. C., and Fahrig, W F., Eds., Mafic dyke swarms: Geological Association of Canada Special Paper **34**, 317–330.
Reid, A. B., Allsop, J. M., Granser, H., Millett, A. J., and Somerton, I. W., 1990, Magnetic interpretation in three dimensions using Euler deconvolution: Geophysics, **55**, 80–91.
Thompson, D. T., 1982, EULDPH—A new technique for making computer-assisted depth estimates from magnetic data: Geophysics, **47**, 31–37.
Wilson, A. H., and Prendergast, M. D., 1988, The Great Dyke of Zimbabwe—1: Tectonic setting, stratigraphy, petrology, structure, emplacement and crystallization, *in* Prendergast, M. D., and Jones, M. J., Eds., Magnetic sulphides—The Zimbabwe volume: Institute of Mining and Metalurgy, 1–20.
Worst, B. G., 1960, The Great Dyke of Southern Rhodesia: Southern Rhodesia Geological Survey Bulletin, **47**.
Zhang, C., Mushayandebvu, M. F., Reid, A. B., Fairhead, J. D. and Odegard, M. E., 2000, Euler deconvolution of tensor gradient gravity data: Geophysics, **65**, 512–520.